

Jake J. Abbott

Institute of Robotics and Intelligent Systems,
ETH Zurich, 8092 Zurich, Switzerland
and

Department of Mechanical Engineering,
University of Utah, Salt Lake City, UT 84112, USA
jake.abbott@utah.edu

Kathrin E. Peyer

Institute of Robotics and Intelligent Systems,
ETH Zurich, 8092 Zurich, Switzerland

Marco Cosentino Lagomarsino

Department of Physics, University of Milan,
20133 Milan, Italy

Li Zhang

Institute of Robotics and Intelligent Systems,
ETH Zurich, 8092 Zurich, Switzerland

Lixin Dong

Institute of Robotics and Intelligent Systems,
ETH Zurich, 8092 Zurich, Switzerland
and
Department of Electrical and Computer Engineering,
Michigan State University, East Lansing, MI 48824, USA

Ioannis K. Kaliakatsos

Bradley J. Nelson

Institute of Robotics and Intelligent Systems,
ETH Zurich, 8092 Zurich, Switzerland
Institute of Robotics and Intelligent Systems,
ETH Zurich, 8092 Zurich, Switzerland
and
Department of Mechanical Engineering,
University of Utah, Salt Lake City, UT 84112, USA

How Should Microrobots Swim?

Abstract

Microrobots have the potential to dramatically change many aspects of medicine by navigating through bodily fluids to perform targeted

diagnosis and therapy. Researchers have proposed numerous micro-robotic swimming methods, with the vast majority utilizing magnetic fields to wirelessly power and control the microrobot. In this paper, we compare three promising methods of microrobot swimming (using magnetic fields to rotate helical propellers that mimic bacterial flagella, using magnetic fields to oscillate a magnetic head with a rigidly attached elastic tail, and pulling directly with magnetic field gradients) considering practical hardware limitations in the generation of magnetic fields. We find that helical propellers and elastic tails have very comparable performance, and they generally become more

The International Journal of Robotics Research
Vol. 00, No. 00, 2009, pp. 000–000
DOI: 10.1177/0278364909341658
© The Author(s), 2009. Reprints and permissions:
<http://www.sagepub.co.uk/journalsPermissions.nav>
Figures 1, 3, 5–10 appear in color online: <http://ijr.sagepub.com>

desirable than gradient pulling as size decreases and as distance from the magnetic-field-generation source increases. We provide a discussion of why helical propellers are likely the best overall choice for *in vivo* applications.

KEY WORDS—microrobot, magnetic, wireless, untethered, medical, *in vivo*

1. Introduction

Microrobots have the potential to dramatically change many aspects of medicine by navigating through bodily fluids to perform targeted diagnosis and therapy. Microrobots, like microorganisms, swim in a low-Reynolds-number regime, requiring swimming methods that differ from macroscale swimmers. Microrobots can also vary in size by orders of magnitude. Researchers have proposed numerous microrobotic swimming methods, many biomimetic, with the vast majority utilizing magnetic fields to wirelessly power and control the microrobot. At ETH Zurich we have developed two different magnetic microrobots that utilize very different propulsion schemes: one is a submillimeter-sized device that is pulled with magnetic field gradients (see Figure 1(a) and Yesin et al. (2006)); the other has a helical propeller that mimics a bacterial flagellum in both form and scale and is rotated with a magnetic field (see Figure 1(b) and Zhang et al. (2009)). Another propulsion scheme proposed in the literature utilizes an elastic tail that is wiggled behind a magnetic head (Sudo et al. 2006; Guo et al. 2008). It remains unclear which propulsion method is optimal, and a comparison that considers the microrobot's size coupled with the practical limitations in generating magnetic fields is needed. In this paper, we compare these three propulsion methods, which are representative of the majority of active research in wireless microrobots. We show that metrics of efficiency, which are often used to characterize low-Reynolds-number swimming, can be quite misleading, and that practical limitations in magnetic control have a major impact on which method is best for a given application. We show that helical propellers and elastic tails have very comparable performance, and they generally become more desirable than gradient pulling as size decreases and as distance from the magnetic-field-generation source increases. We also find that limitations in the hardware used to generate the magnetic fields can influence which swimming method is best. In the end, we provide a discussion of why helical propellers are likely the best overall choice for *in vivo* applications.

2. Swimming at Low Reynolds Number

It has long been known that swimming at the microscale requires techniques that are very different from those used by macroscale swimmers such as fish and humans (Purcell 1977).

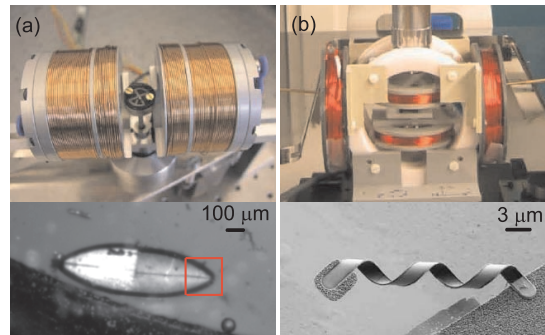


Fig. 1. Swimming microrobots with a 30:1 size difference. Magnetic fields are used to: (a) pull a 900- μm -long assembled-MEMS microrobot (Yesin et al. 2006); and (b) rotate a 30- μm -long artificial-bacterial-flagella microrobot (Zhang et al. 2009).

To understand this phenomenon, we turn to the Navier–Stokes equations, which, when combined with boundary conditions, completely define a fluid flow. For a fluid with constant density ρ and constant viscosity η , the Navier–Stokes equations are given by a single vector equation, which can be non-dimensionalized in space and time by the magnitude of some characteristic velocity U and some characteristic length δ :

$$\left(\frac{\rho U \delta}{\eta}\right) \frac{d\tilde{\mathbf{V}}}{dt} = -\nabla \tilde{p} + \nabla^2 \tilde{\mathbf{V}} \implies Re = \frac{\rho U \delta}{\eta}. \quad (1)$$

Here $\tilde{\mathbf{V}}$ is the velocity vector field and \tilde{p} is the hydrodynamic pressure scalar field, which have both been non-dimensionalized as in White (1991). From this equation we discover the Reynolds number, the dimensionless quantity that embodies the interaction between a fluid's inertia and viscosity. At low Re , we are in a world that is very viscous, very slow, or very small. Low- Re flow around a body is referred to as creeping flow or Stokes flow. We no longer see a transition to turbulence, even behind bluff bodies. At low Re , the role of time becomes negligible in (1); the flow pattern does not change appreciably whether it is slow or fast, and the flow is effectively reversible. Consequently, reciprocal motion (i.e. body motion that simply goes back and forth between two configurations) results in negligible net movement.

Microorganisms are able to swim at low Re using a variety of techniques (Brennen and Winet 1977; Vogel 2003; Lauga and Powers 2009), none of which look like macroscale swimmers (Figure 2). Cilia are active organelles that are held perpendicular to the flow during the power stroke and parallel to the flow during the recovery stroke. Many cilia are used simultaneously. Eukaryotic flagella are active organelles that deform to create paddling motions, such as traveling waves or circular translating movements. Bacterial (prokaryotic) flagella work differently by using a molecular motor to turn the base of a

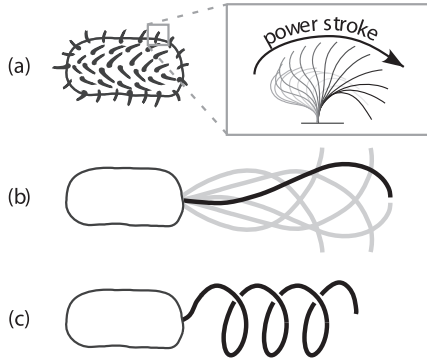


Fig. 2. Locomotion of microorganisms. The cells are drawn identically to highlight the differences in the propulsion methods, but there is a wide range of shapes and sizes of microorganisms. (a) Cilia move across the flow during the power stroke, and fold near the body during the recovery stroke. (b) Eukaryotic flagella create patterns such as traveling waves. (c) A molecular motor spins a passive bacterial flagella.

passive flagellum. Some bacteria have multiple flagella that bundle during swimming. All of the swimming methods utilized by microorganisms capitalize on the difference in drag on a slender body normal and parallel to the slender direction as it is pulled through fluid. All of the methods are fairly inefficient (efficiency is discussed in detail in Section 7).

A number of robotic swimming methods have been shown to work at relatively small scales, but will have reduced effectiveness as size decreases to the microscale because they make use of reciprocating configurations. Other biomimetic swimming methods utilize physics that scale well to the microscale, but require mechatronic components that present challenges in microfabrication and wireless power and control (Behkem and Sitti 2006; Kósa et al. 2007, 2008). A number of microrobots are inspired by nature and also utilize techniques that facilitate microfabrication and wireless power and control. Nearly every one utilizes magnetic fields (see Figure 3). No other actuation principle offers the ability to transfer such large amounts of power wirelessly. For example, a rotating magnetic field is an obvious choice to rotate a helical propeller (Honda et al. 1996; Zhang et al. 2009), eliminating the need to replicate a molecular motor in a microrobot. However, even with all of their positive attributes, magnetic fields impose strict limitations on the design of wireless microrobots.

A controllable external pulling source is not available to microorganisms, but engineers can utilize gradients in magnetic fields to apply forces and torques to untethered microrobots (Mathieu et al. 2006; Yesin et al. 2006). This greatly simplifies fabrication since no microactuator or special structure is needed for propulsion. Biomimetic methods will clearly be effective, but it is also reasonable to wonder whether this form of direct-pulling propulsion, which could not have evolved

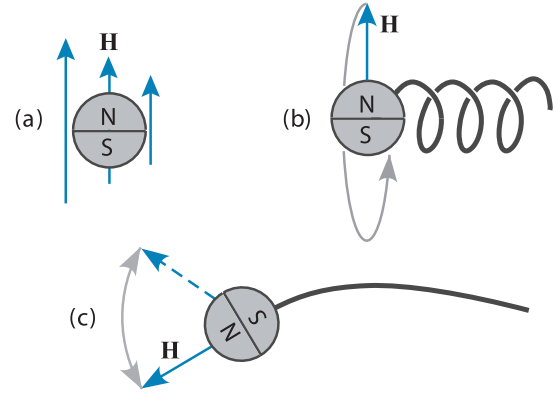


Fig. 3. Magnetic swimming methods. In each case, the microrobot is swimming from right to left. In each case, the entire microrobot body is depicted as a magnet, but it is also possible for the magnet to be rigidly embedded in a larger body. (a) Gradients in the magnetic field pull the microrobot directly. (b) A rotating uniform magnetic field is transduced into forward motion using a helical propeller. (c) An oscillating uniform magnetic field is transduced into forward motion using an elastic tail.

through natural selection, might outperform biomimetic methods.

3. Magnetic Power and Control

If we want to apply controlled forces and torques to a body with average magnetization \mathbf{M} using a controlled magnetic field \mathbf{H} (both quantities are vectors in amps per meter), the governing control equations are as follows (Jiles 1991). The magnetic torque tends to align the magnetization of the body with the applied field:

$$\mathbf{T} = \mu_0 \vartheta \mathbf{M} \times \mathbf{H}, \quad (2)$$

where ϑ is the volume of the body in cubic meters and $\mu_0 = 4\pi \times 10^{-7} \text{ T}\cdot\text{m A}^{-1}$ is the permeability of free space (here the non-bold T represents the unit Tesla). The magnetic force on the body is

$$\mathbf{F} = \mu_0 \vartheta (\mathbf{M} \cdot \nabla) \mathbf{H}. \quad (3)$$

We can also express the applied magnetic field as an applied magnetic flux density \mathbf{B} in Tesla. Here \mathbf{B} is related to \mathbf{H} simply as $\mathbf{B} = \mu_0 \mathbf{H}$, since air and biological materials are effectively non-magnetic. Both (2) and (3) are based on the assumption that the magnetic body is small compared with spatial changes in the applied field, such that the applied field is fairly uniform across the body, and \mathbf{H} is the value of the applied field at the center of mass of the body. We have verified in prior work that this assumption gives an accurate prediction of magnetic force and torque (Abbott et al. 2007; Nagy et al. 2008).

If the body of interest is a permanent magnet, the average magnetization \mathbf{M} is effectively constant with respect to the body with a magnitude governed by the remanent magnetization of the material. We can increase torque by increasing the angle between \mathbf{H} and \mathbf{M} , up to 90° , or by increasing the strength of \mathbf{H} . We can increase force by increasing the gradients in the applied field. If the body of interest is made of a soft-magnetic material, the magnetization is a non-linear function of the applied field, with a magnitude bounded from above by the saturation magnetization value for the material, and can rotate with respect to the body; the governing equations for control are significantly more complex (Abbott et al. 2007; Nagy et al. 2008). We sometimes refer to the “magnetic moment” or “magnetic dipole moment”, which represent the total strength of a magnet (permanent or soft). The magnetic moment is simply the product of the volume ϑ and the average magnetization \mathbf{M} .

Every magnetic body has geometric effects that make its magnetic properties differ from those of the bulk material and different along different directions within the body. This is known as shape anisotropy. Demagnetizing fields are created that tend to weaken magnetization, and demagnetizing fields are largest along short directions of the body. A long direction in a body is referred to as an easy axis, since it is a relatively easy direction in which to magnetize the material. Other types of anisotropy exist, such as crystalline anisotropy, but these are typically negligible compared with shape effects, even at the scale of microrobots.

Controlled magnetic fields can be generated by stationary current-controlled electromagnets (Meeker et al. 1996; Zhang et al. 2009), such as the system shown in Figure 1(b), by electromagnets that are position and current controlled (Grady et al. 1990; Yesin et al. 2006), such as the system shown in Figure 1(a), by position-controlled permanent magnets, such as with the Stereotaxis Niobe Magnetic Navigation System, or even by a commercial magnetic resonance imaging (MRI) system (Mathieu et al. 2006). In all cases, the rapid decay of magnetic field strength with distance from its source creates a major challenge for magnetic control.

4. Pulling Through Fluid with Field Gradients

The first method of wireless magnetic swimming that we consider is simply pulling a rigid object through fluid using magnetic field gradients, which is depicted in Figure 3(a). Although this is a valid method to actively move through fluid that we would like to consider, it is not technically “swimming” since it does not use the fluid to assist in propulsion. When pulling a magnetic object through Newtonian fluid at low Re , the object nearly instantaneously reaches its terminal velocity \mathbf{V} where the viscous drag force, which is linearly related to velocity through a drag coefficient ψ_v , exactly balances the applied magnetic force \mathbf{F} :

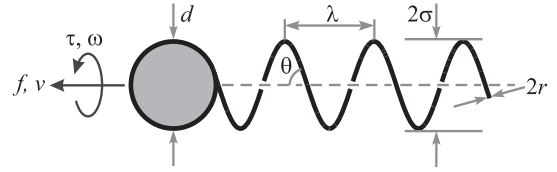


Fig. 4. Definition of parameters for a microrobot with a helical propeller with right-handed chirality. The force f and torque τ represent the sum of all non-fluidic loads.

$$\mathbf{F} = \psi_v \mathbf{V}. \tag{4}$$

If we consider a spherical bead of diameter d , the translational drag coefficient is described in Stokes flow (see White (1991)) as

$$\psi_v = 3\pi\eta d. \tag{5}$$

It is clear that velocity is inversely proportional to fluid viscosity with all other parameters held constant.

The magnetic force of (3) also simplifies in the case of a soft-magnetic spherical bead to

$$\mathbf{F} = \mu_0\vartheta[\mathbf{M}(\nabla|\mathbf{H})]. \tag{6}$$

This equation also applies to a permanent magnet under the assumption that the magnetization \mathbf{M} is always aligned with the applied field \mathbf{H} .

5. Swimming with a Helical Propeller

The next method of wireless magnetic swimming that we consider is swimming with a helical propeller, which is depicted in Figure 3(b). Consider the helical propeller with parameters defined as shown in Figure 4. Swimming along the axis of a helical propeller is described by a symmetric propulsion matrix (Purcell 1977, 1997) relating the four principle (scalar) quantities, forward velocity v , angular velocity ω , non-fluidic applied torque τ , and non-fluidic applied force f , of the helical propeller:

$$\begin{bmatrix} f \\ \tau \end{bmatrix} = \begin{bmatrix} a & b \\ b & c \end{bmatrix} \begin{bmatrix} v \\ \omega \end{bmatrix}, \tag{7}$$

where the matrix parameters are computed as

$$a = 2\pi n\sigma \left(\frac{\xi_{\parallel} \cos^2\theta + \xi_{\perp} \sin^2\theta}{\sin\theta} \right), \tag{8}$$

$$b = 2\pi n\sigma^2 (\xi_{\parallel} - \xi_{\perp}) \cos\theta, \tag{9}$$

$$c = 2\pi n\sigma^3 \left(\frac{\xi_{\perp} \cos^2\theta + \xi_{\parallel} \sin^2\theta}{\sin\theta} \right), \tag{10}$$

where n is the number of turns of the helix (such that the helix length is $n\lambda$), and the constants ζ_{\perp} and ζ_{\parallel} are the viscous drag coefficients for a thin cylindrical element of a helical propeller for flow locally normal to the cylinder's axis and along the length of the cylinder's axis, respectively, given by Lighthill (1976) as

$$\zeta_{\perp} = \frac{4\pi\eta}{\ln\left(\frac{0.36\pi\sigma}{r\sin\theta}\right) + 0.5} \quad (11)$$

$$\zeta_{\parallel} = \frac{2\pi\eta}{\ln\left(\frac{0.36\pi\sigma}{r\sin\theta}\right)} \quad (12)$$

The effect of the rigidly attached head is to modify the propulsion matrix of the helical propeller of (7) to

$$\begin{bmatrix} f \\ \tau \end{bmatrix} = \begin{bmatrix} a + \psi_v & b \\ b & c + \psi_{\omega} \end{bmatrix} \begin{bmatrix} v \\ \omega \end{bmatrix}, \quad (13)$$

where ψ_v and ψ_{ω} are translational and rotational drag coefficients for the head, respectively. If we consider a spherical head, the rotational drag coefficient is described in Stokes flow (see White (1991)) as

$$\psi_{\omega} = \pi\eta d^3 \quad (14)$$

and the translational drag coefficient is given in (5).

In the case of magnetically applied torques, the rotational frequency of the magnetic field is the fundamental control input. The microrobot rotates synchronously with the applied field, nearly instantaneously reaching an equilibrium phase shift such that the magnetic torque perfectly counterbalances the fluidic drag torque. It is more instructive in this case to rearrange the linear equations with the non-fluidic applied force f and angular velocity ω as the input variables:

$$\begin{bmatrix} v \\ \tau \end{bmatrix} = \begin{bmatrix} \alpha & \beta \\ -\beta & \gamma \end{bmatrix} \begin{bmatrix} f \\ \omega \end{bmatrix}, \quad (15)$$

where (13) and (15) are related by

$$\alpha = \frac{1}{a + \psi_v}, \quad \beta = \frac{-b}{a + \psi_v}, \quad (16)$$

$$\gamma = c + \psi_{\omega} - \frac{b^2}{a + \psi_v}.$$

Figure 5 shows the behavior observed with this type of swimming. The forward velocity grows linearly with frequency until a step-out frequency is reached. Beyond this step-out frequency, the available magnetic torque is no longer sufficient to keep the microrobot rotating in sync with the applied field, and a drastic and non-deterministic decrease in the swimming velocity is observed. This behavior has been demonstrated experimentally at a number of scales (Honda et al. 1996; Zhang

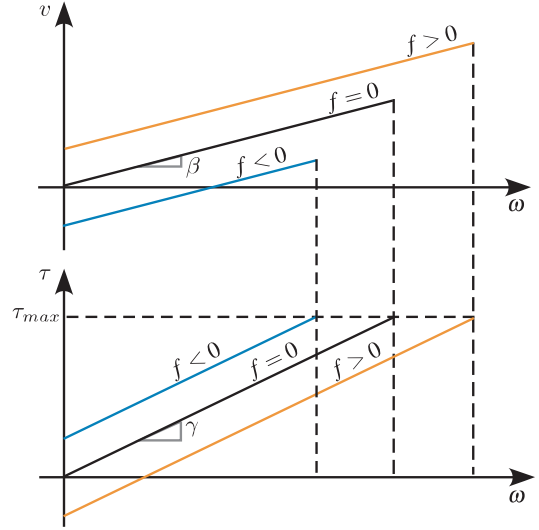


Fig. 5. Qualitative behavior of helical-propeller swimming, with rotational frequency as the control variable, which is particularly useful when considering helical propellers driven by applied magnetic fields. Parameters are defined in (15) and Figure 4.

et al. 2009). The step-out frequency is a function of τ_{\max} , the maximum magnetic torque that can be generated as described in (2), as depicted in Figure 5.

It is notable that the fluid viscosity η enters into (8)–(10) linearly. Consequently, η enters into γ linearly, but does not enter into β . Taking this into consideration, from Figure 5 we find that the effect of doubling viscosity with all other parameters held constant would be to reduce the step-out frequency by half and, consequently, to reduce the maximum velocity by half. That is, the maximum velocity is inversely proportional to fluid viscosity.

6. Swimming with an Elastic Tail

The final method of wireless magnetic swimming that we consider is swimming with an elastic tail (sometimes referred to as a “flexible oar”), which is depicted in Figure 3(c). A magnetic field is oscillated in time, and a magnetic torque is applied to the magnetic head as it attempts to align with the applied field. There have been a few experimental demonstrations of this type of microrobot swimming (Sudo et al. 2006; Guo et al. 2008), but the deformable nature of the elastic tail makes even basic analysis of this type of swimming significantly more complicated than that of the rigid helical propeller, and there currently exists no analytical model for this method. The closest is the free-swimming elastic tail being driven by a pure torque at one end considered analytically for small deformations in Wiggins and Goldstein (1998) and numerically for

large deformations in Cosentino Lagomarsino et al. (2003), with the differences to the case of Figure 3(c) being that in their case a constraint on a fixed angular deflection was considered, and that the application of the torque had no associated additional viscous effects (i.e. no increased drag due to an increased magnetic bead size associated with an increase in magnetic torque). The same authors also considered the case where the end of an elastic filament is driven with an oscillating lateral movement of fixed amplitude (Wiggins and Goldstein 1998; Wiggins et al. 1998; Cosentino Lagomarsino et al. 2003).

Let us consider the case of the elastic tail driven by a pure oscillating torque described by $\tau = \tau_0 \sin(\omega t)$. The elastic tail has a length l , a bending stiffness κ , and a perpendicular viscous drag coefficient of ζ_{\perp} . We are interested in the net swimming velocity v . From dimensional analysis, we find that the dimensionless velocity

$$\mathcal{V} = \frac{v}{\omega l} \tag{17}$$

is a function of two dimensionless parameters: one is commonly referred to as the Sperm number

$$Sp = l \left(\frac{|\omega| \zeta_{\perp}}{\kappa} \right)^{1/4}, \tag{18}$$

which encapsulates the waveform, or ‘‘floppiness’’, of the tail, and the other is the dimensionless torque magnitude

$$\mathcal{T} = \frac{\tau_0 l}{\kappa}. \tag{19}$$

Figure 6(a) shows the results of numerical simulations using the same methods as presented in Cosentino Lagomarsino et al. (2003). It shows how \mathcal{V} varies with Sp for various values of constant \mathcal{T} . We find that \mathcal{T} affects \mathcal{V} linearly, which allows us to plot a single dimensionless quantity \mathcal{V}/\mathcal{T} as a function of Sp in Figure 6(b). The results indicate that a peak value in dimensionless velocity occurs at $Sp \approx 4.3$, regardless of the value of \mathcal{T} .

For a simple model of bending stiffness, we can consider that of a cylindrical beam of radius r and Young’s modulus E :

$$\kappa = \frac{\pi r^4 E}{4}. \tag{20}$$

From Vogel (2003), an appropriate value for ζ_{\perp} in this case is

$$\zeta_{\perp} = \frac{4\pi \eta}{\ln \left(\frac{l}{r} \right) + 0.193}. \tag{21}$$

7. A Critical Comparison

In order to make a fair comparison between microrobots that utilize magnetic fields in different ways, we must consider the

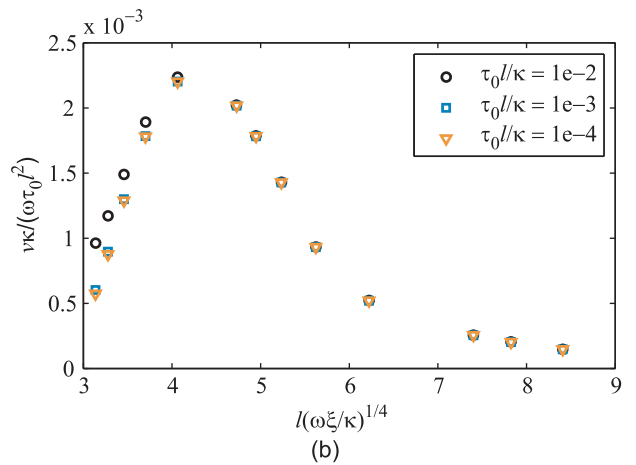
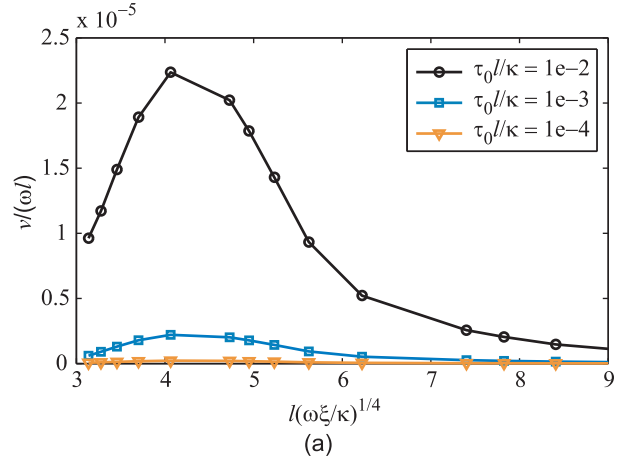


Fig. 6. Dimensionless results for numerical simulations of an elastic tail being driven by a pure sinusoidal torque at one end. (a) Dimensionless velocity versus the Sperm number for various value of constant dimensionless torque. (b) Dimensionless velocity normalized by dimensionless torque versus the Sperm number, showing that dimensionless torque affects dimensionless velocity linearly.

hardware that generates the magnetic field. In practice, there will be limits to how close the field sources can be placed to the microrobot. Let us compare the control of a microrobot with two current-carrying coils, as shown in Figure 7. Our field sources are assumed to be located a distance L from our microrobot. The limitations imposed by this two-coil system are representative of other magnetic control systems, such as those as described in Section 3.

7.1. Helical Propeller versus Gradient Pulling

We begin by comparing swimming with a helical propeller to simply pulling with field gradients. We assume a simple mag-

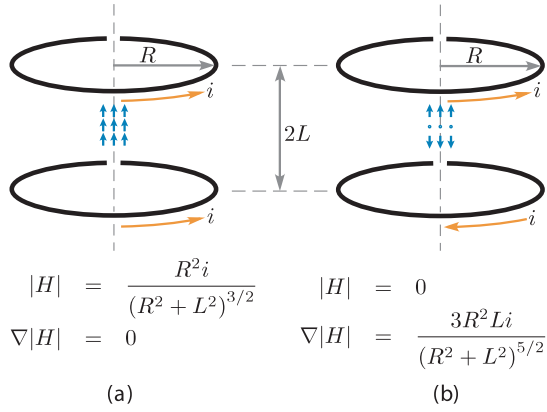


Fig. 7. Two electromagnetic coils as field-generation hardware for microrobot propulsion. (a) Uniform magnetic fields in the center of the workspace are generated by current flowing in the same direction. The field is calculated accurately with a current-loop model along the axis of the coils (Jiles 1991). (b) Gradient fields can be generated by running the current in opposite directions.

netic bead of diameter d for our microrobot. We have two options for control: we can attach a helical propeller to our bead and then apply current in the same direction in the two loops, creating a uniform field that is used to rotate and thus propel the bead; or we can apply the current in opposite directions, creating a field gradient that is used to pull on the bead directly. From the equations that describe the magnetic field and field gradient at the midpoint of the current loops, shown in Figure 7, we see that the field that we can generate changes with the gap between the two loops as $\sim L^{-3}$, while the gradient that we can generate changes as $\sim L^{-4}$, as expected. We also find that there are optimal values for the coil radii for a given coil gap to maximize the respective quantities: $R = \sqrt{2}L$ for case (a) and $R = \sqrt{2/3}L$ for case (b).

In Figure 8 we plot the maximum no-load ($f = 0$) velocity and the maximum stall ($v = 0$) force versus bead size. For the helical parameters, we choose $\sigma = d/2$, $r = d/200$, and $\theta = 45^\circ$. For the coil gap, we assume $L = 0.2$ m, which is the approximate value that would be needed to control a microrobot somewhere inside a human head. To avoid biasing the results, we use the optimal radii R for the respective cases. The results for two helices are shown: one for $n = 3$ and one for $n = 10$. The magnetization of the bead and the current through the loops enter into the maximum velocity and force linearly, so we can normalize our results to these quantities. The reciprocal of viscosity enters into the maximum velocity linearly, so we can normalize to this quantity as well; the viscosity has no bearing on the maximum force.

We find that the maximum velocity varies as $\sim d$ for helical propulsion and as $\sim d^2$ for pulling. We find that the max-

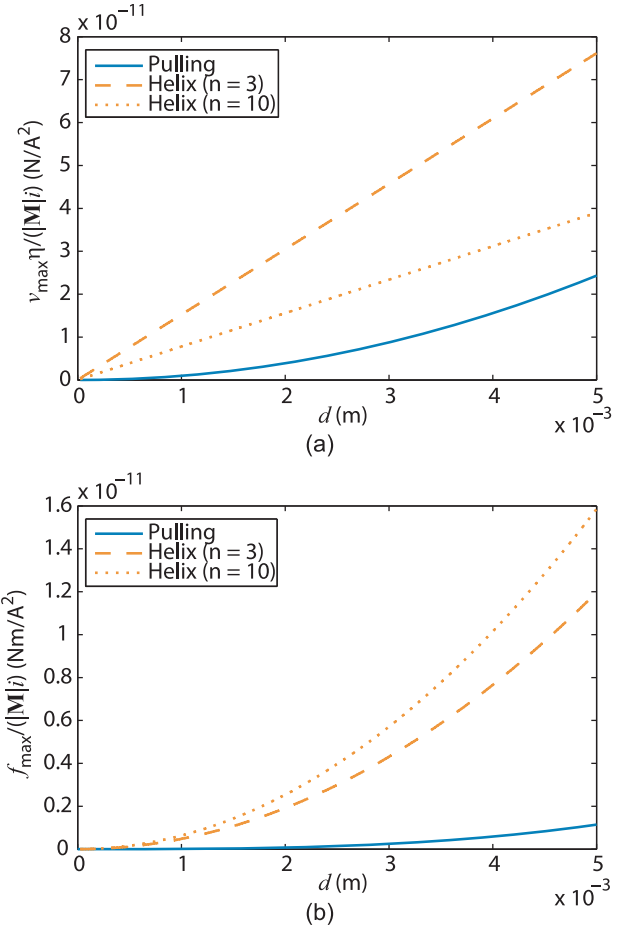


Fig. 8. Comparison of (a) normalized no-load ($f = 0$) velocity and (b) normalized stall ($v = 0$) force vs. bead radius for helical propulsion and field-gradient pulling.

imum force varies as $\sim d^2$ for helical propulsion and as $\sim d^3$ for pulling. This indicates that there will always exist a microrobot size below which using helical propulsion is desirable over pulling with field gradients. In addition, even though the helical parameters used here were not optimized, Figure 8 indicates that helical propulsion is desirable (by a large margin) over pulling for any microrobot size that would reasonably be considered as microscale. In addition, increasing the distance between the magnetic field sources and the microrobot (i.e. L), which will likely be necessary for *in vivo* applications, will always tend to improve helical propulsion relative to pulling, although the effectiveness of both will be reduced.

Although helical propulsion of a body is described as being quite inefficient compared with simply pulling the body through the fluid (Purcell 1977, 1997), this is misleading in the context of magnetic control. Purcell uses a definition of swimming efficiency that compares the power used to propel a body at a given velocity and the power re-

quired to simply pull the body through the fluid at the same velocity:

$$\varepsilon = \frac{\text{power required to simply pull body}}{\text{power consumed during propulsion}}. \quad (22)$$

Under this definition of efficiency, pulling with field gradients is 100% efficient (i.e. $\varepsilon = 1$), and every other swimming method will always perform less efficiently. The problem with this definition in this context is that the amount of power that can be harvested from the applied magnetic field is different in each of our cases, so a comparison of the efficient use of that power does not give meaningful results.

Theoretical models of microrobot swimming should be improved, but the discrepancy between the models at the microscale observed in Figure 8 might be too large to be drastically affected by improved models. However, there is another practical limitation in the magnetic control of helical swimmers that we must consider. Our actual control variable is the rotation frequency ω of the magnetic field. As described in Section 5, the microrobot rotates in sync with the field, with the field leading the magnetization such that the magnetic torque from (2) balances the viscous torque. As ω is increased, the magnetic torque eventually reaches its step-out frequency, above which the microrobot can no longer track the rotating field. The maximum velocity and force curves of Figure 8 assume that the microrobot is turning at its step-out frequency, which also increases linearly with the quantity $|\mathbf{M}|i/\eta$. For any field-generation system, there are practical saturation limits in generating high ω due to, for example, induction, eddy currents, motor speeds, or sampling rates. If this ω -saturation is reached, the values shown in Figure 8 will over-estimate the capabilities of helical propulsion. We must also recall that the propulsion model implicitly assumes low- Re flow, which could be violated for very high ω . Thus, although it is always desirable to increase $|\mathbf{M}|$ and i for improved control using either swimming method, it could reduce the performance of helical propulsion relative to pulling. It should be noted, however, that the step-out frequency is scale invariant (discussed more in the next section), and published experimental results for helical swimmers have typically had step-out frequencies below 60 Hz, indicating that this high- ω problem is unlikely to significantly impact on our conclusions.

7.2. Helical Propeller versus Elastic Tail

To compare helical-propeller swimming with elastic-tail swimming in the context of wireless magnetic control, we make use of the fact that both methods transduce mechanical power from the applied magnetic field in the same way: through magnetic torque. So, for a given magnetic bead driven by either type of propeller, we can simply assume some maximum available torque τ_{\max} available to the microrobot, which is a function of the bead geometry and material as well as

the field-generation hardware, and is governed by (2). Neither swimming method relies on field gradients, which means that both methods will improve relative to gradient pulling as the distance to the field-generation hardware is increased.

Let us consider an elastic tail driven by a pure sinusoidal torque at one end, as detailed in Section 6. We assume that the tail is being driven optimally, and that we are making use of the available magnetic torque such that $\tau_0 = \tau_{\max}$. Although the peak in dimensionless velocity in Figure 6 occurs at $Sp \approx 4.3$, this is not the location of peak velocity, due to the way that ω affects both \mathcal{V} and Sp . We find that velocity is actually optimized when $Sp^4 \mathcal{V}$ is maximized, which we find occurs at $Sp \approx 5.2$, and which corresponds to

$$\frac{v\kappa}{\omega\tau_0 l^2} = 1.4 \times 10^{-3}. \quad (23)$$

After some substitutions, we can express the maximum swimming velocity as

$$v_{\max} = \left(\frac{1.0}{\xi_{\perp} l^2} \right) \tau_{\max}. \quad (24)$$

With an understanding that the maximum magnetic torque will scale with the volume of material, and with all other parameters held constant, we find that v_{\max} scales with microrobot size as $\sim l$. We also find that v_{\max} is inversely proportional to fluid viscosity. We can also consider the case of a helical propeller being driven by a pure torque. For the helical propeller of (7), we compute

$$v_{\max} = \left(\frac{b}{b^2 - ac} \right) \tau_{\max}. \quad (25)$$

We again find that v_{\max} scales with microrobot size as $\sim l$, and that v_{\max} is inversely proportional to fluid viscosity.

The performance of both helical propellers and elastic tails scale in the same way. However, we have not yet considered how the driving frequency ω changes with scale. To maintain the elastic tail swimmers running at peak performance, we must achieve

$$\omega = \frac{\kappa}{\xi_{\perp}} \left(\frac{5.2}{l} \right)^4. \quad (26)$$

Assuming that the stiffness κ varies as $\sim l^4$ (see (20)), we find that the peak value for ω does not change as we scale the elastic-tail microrobot. If, however, the length of the tail is changed without changing the cross section, we find that ω varies as $\sim l^{-4}$, which would lead to a significant increase in optimal driving frequency if we shorten the length of the tail. For the helical-propeller swimmer, for optimal performance we must run the swimmer at the step-out frequency, which is the maximum frequency ω_{\max} that can be achieved for a given τ_{\max} , and which is described in free swimming by

$$\omega_{\max} = \left(\frac{a}{ac - b^2} \right) \tau_{\max}. \quad (27)$$

For the helical-propeller, we find that the driving frequency does not change as we scale the microrobot size.

We have shown that the performance of these two methods of microrobot swimming scale identically to one another, assuming the cross section of the elastic tail scales proportionally to all other parameters. This means that if one type of propulsion outperforms the other, it will always outperform, regardless of scale. However, we would still like to know which, if either, swimming method is superior. To do this, let us consider an example. If we construct a 2-mm-long helical swimmer with a pitch of $\theta = 45^\circ$, four turns, and a cross section with $r = 50 \mu\text{m}$, we compute a maximum velocity of $v_{\text{max}} = (7.7 \times 10^4)\tau_{\text{max}}/\eta$, with a corresponding angular velocity of $\omega_{\text{max}} = (7.3 \times 10^9)\tau_{\text{max}}/\eta$. Note that both τ_{max} and the reciprocal of fluid viscosity enter into these terms linearly, and can therefore be factored out. For an elastic-tail swimmer with 2-mm length and a cross section with $r = 50 \mu\text{m}$, we again calculate $v_{\text{max}} = (7.7 \times 10^4)\tau_{\text{max}}/\eta$. It is a coincidence that these two peak-velocity values are identical, and we find that by varying parameters we can make either type of microswimmer outperform the other. However, this example does give us an indication that we should expect similar peak performance from these two types of microswimmers, assuming the same length and the same maximum magnetic torque. We have compared our numerical models with prior experimental results (Sudo et al. 2006; Zhang et al. 2009) and find excellent agreement. These prior experiments also indicate that optimal driving frequencies are comparable between the two types of microswimmers, and also feasible from a hardware standpoint (e.g. 30–60 Hz).

It may be the case that comparing microswimmers of the same length biases the comparison in favor of the helical propeller. In some cases it may be acceptable to shorten the length of the elastic tail to increase the forward velocity, as indicated in (24). However, we know that this shortening may drastically increase the driving frequency, as indicated in (26).

In our comparison of peak velocity, we found that τ_{max} could be factored out for both microswimmers. However, we find that the optimal ω for helical propulsion is linearly affected by the non-scale-related contribution of τ_{max} (i.e. the field strength and the magnetization of the material), whereas the optimal ω for elastic tails is completely independent of τ_{max} . This indicates that, as we reduce the strength of the applied magnetic field, the optimal driving frequency of the helical swimmer will reduce relative to that of the elastic-tail swimmer, which may be desirable from a hardware and control standpoint.

8. Discussion

It appears that, under some reasonable simplifying assumptions, helical-propeller microrobots and elastic-tail microrobots have very comparable peak performance, and both will

outperform field-gradient-pulled microrobots once we consider the practical limitations involved in generating magnetic fields.

From a fabrication standpoint, constructing an elastic-tail microswimmer seems feasible, considering the relatively simple design. However, this has not been done to date (prior experiments have considered up-scaled models), and it is not clear which materials would be the best choice for the tail. It has already been shown that it is possible with currently available technology to microfabricate helical-propeller magnetic microrobots (Zhang et al. 2009). This has been accomplished with nanocoils, which are rolled-up pre-stressed multilayer strips. This technique has better control over helical geometry than grown helical carbon nanotubes or ZnO nanobelts. The radius of the coil is determined by the thicknesses of the films, the Young's moduli of the materials, and the lattice mismatches of the layers. Figure 9(a) shows the process sequence to fabricate nanocoil microrobots, which consist of a 42-nm-thick ribbon that, upon wet etch release, self-forms into a 3- μm -diameter coil with a length of 30–40 μm . A 4.5 $\mu\text{m} \times 4.5 \mu\text{m} \times 0.2 \mu\text{m}$ Ni plate is formed on one end that serves as a “head”. The geometrical relation of the nanocoil parameters is shown in Figure 9(b). The width of the stripe is given by its initial pattern design, and the depth is controlled during fabrication. Figure 9(c) shows a scanning electron microscopy (SEM) image of an as-fabricated nanocoil with a Ni plate on one end. For a first propulsion experiment, individual magnetic nanocoils were immersed in water, actuated with a rotating magnetic field (see hardware in Figure 1(b)), and their motion was captured on video through a microscope. One sequence for a 40- μm -long nanocoil is shown in Figure 9(d).

Microrobots that swim using helical propellers have a number of additional potential benefits for use as *in vivo* medical devices that we believe makes them the most promising as a technology worth pursuing. They include the following.

1. Reversing direction is simple with a rigid helical propeller. It simply entails reversing the rotation direction of the magnetic field. This could be particularly useful in retracing a path already taken. Microrobots that are pulled with field gradients are also easily reversed. However, to reverse the swimming direction of an elastic-tail microrobot, the microrobot must turn completely around, which is less efficient and potentially more difficult to accomplish.
2. A rigid helical propeller can be functionalized (e.g. coated) without significantly changing its fluid-dynamic properties. This is not likely true of an elastic tail, whose bending properties will change due to functionalization. Adding extra fluid drag will always reduce performance with gradient-pulling methods. It has also been suggested that the microrobot's payload, such as a strip of

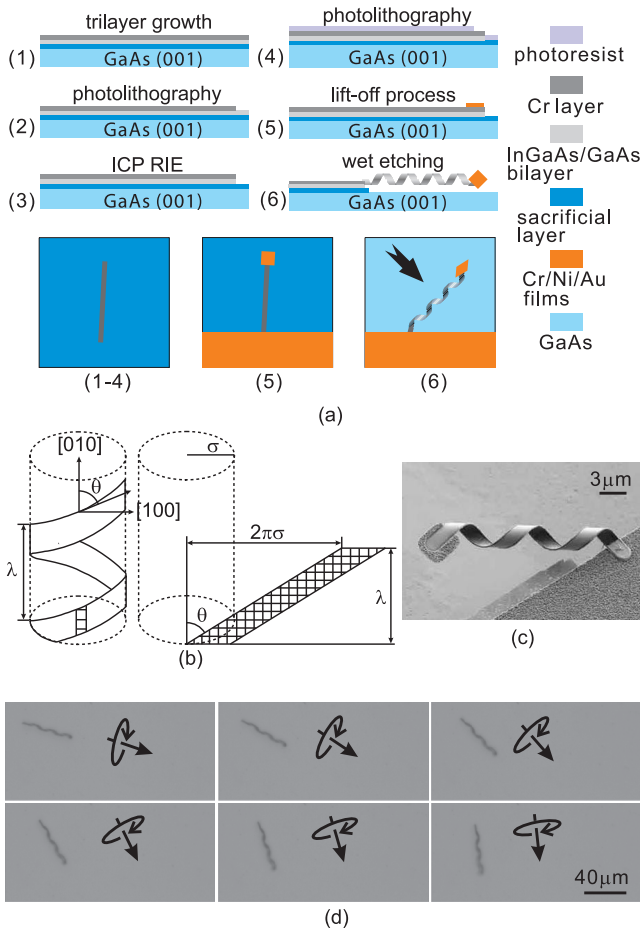


Fig. 9. Nanocoils as artificial bacterial flagella (Zhang et al. 2009). (a) Microfabrication process sequence: an initially planar epitaxial trilayer with a plate on one end consisting largely of soft-magnetic Ni, all patterned through conventional microfabrication techniques, self-forms into a three-dimensional structure during wet etch release. (b) Schematic drawing showing the relationship between the stripe and etching direction in nanocoil parameters. (c) SEM image of an as-fabricated micro-robot. (d) Optical microscope image sequence of a microrobot swimming in water. Arrows indicate the forward direction and corresponding rotation being commanded by the electromagnetic system.

drug, can be twisted up into a helical propeller to actually contribute to propulsion (Li et al. 2006). An elastic tail might also be made of drug, provided the elasticity and stiffness of the drug can be fabricated correctly.

3. Microrobots that swim using helical propellers have the potential to smoothly transition from lumen to open environments. For example, consider a microrobot designed for use in the urinary system. After insertion into

the urethra, the microrobot crawls toward the bladder by pressing its helical propeller against the partially collapsed walls of the urethra. The microrobot does not swim in this case, but actually crawls forward, ideally advancing by one pitch per rotation, but with the possibility of some amount of slip. This type of helical lumen crawling has been explored previously (Sendoh et al. 2003). Once the microrobot reaches the bladder, it transitions into the type of swimming discussed in this paper. The microrobot could even swim toward the opening of the ureter and transition back to crawling to advance toward the kidney. It is unclear whether an elastic tail or gradient-pulling would be effective inside a lumen whose size is comparable to that of the microrobot and potentially even collapsed. A driven elastic tail makes lateral movements throughout its cycle (with no net lateral movement) as it is propelled forward. A wall constraint, such as a lumen environment, will affect the swimming pattern and performance of an elastic-tail swimmer compared with the model described in Section 6.

4. Swimming with helical propulsion opens up the possibility of control in non-uniform magnetic fields. Although the analysis presented in this paper assumes a uniform (gradient-free) magnetic field, which in practice is developed in the center of two equally powerful electromagnets as depicted in Figure 7(a), it is also possible to swim against magnetic field gradients provided that the propulsive force of the helical propeller is large enough. We have already demonstrated this experimentally with the microrobots of Figure 9 by using the field of a single rotating permanent magnet. This possibility of using non-uniform fields allows us to be more creative in the design of field-generation hardware, and may prove particularly useful in the control of *in vivo* microrobots. Swimming against field gradients may also be possible with an elastic tail, however, the inability to reverse direction easily (discussed above) makes the design of field-generation hardware more challenging. Swimming against a field gradient is never possible with gradient-pulling methods.

5. The same magnetic control system that is designed to control helical swimmers can also be used to control screw-type microrobots, which are microrobots that consist of a magnet rigidly embedded in a microrobot shaped something like a wood screw (Ishiyama et al. 2003). These screw-type microrobots provide a promising method to move through soft tissues such as brain and liver. With the ability to control two types of microrobots with the same hardware, the probability of both of these two technologies taking hold in clinical practice increases, since costs, both in terms of finances and

space, will be distributed over multiple potential procedures.

There are a number of modeling assumptions used in this paper that could be improved to increase the accuracy of the models; the most salient are discussed below. However, it is unlikely that these assumptions will significantly affect the conclusions that we have reached.

1. The model in Section 5 assumes that the head and the helical propeller do not affect each others' flow fields, which clearly cannot be true. The model in Section 6 does not account for any fluid drag on the magnetic head.
2. The individual Stokes-flow models are all derived assuming an infinite extent of fluid. Figure 10 shows magnetic and hydrodynamic data for three steel beads, obtained with a custom measurement system (Kummer et al. 2007). We see that the magnetic models are quite accurate, but the viscous drag coefficient ψ_v for Stokes flow around a sphere is less accurate, due to the wall effects of the container (i.e. fluid viscosity effectively increases nearer to a solid boundary). Wall effects have also been observed to affect helical propulsion (Behkem and Sitti 2006), elastic-tail propulsion (Yu et al. 2006), and are generally important in low- Re swimming (Vogel 2003; Lauga and Powers 2009). From Figure 10(b), the speed of gradient-pulled beads is clearly reduced due to wall effects. The cases of the other two swimmers that we consider are more complicated. The efficiency of both helical-propeller swimmers and elastic-tail swimmers are governed by the ratio of the fluid drag coefficients of the propeller: $\xi_{\perp}/\xi_{\parallel}$. That is, swimming becomes more efficient in cases when the fluid drag for flow perpendicular to an element of the propeller increases relative to fluid drag for flow along an element of the propeller. It has been shown that wall effects tend to increase this drag-coefficient ratio, and thereby increase efficiency (Brennen and Winet 1977). However, this is another use of "efficiency" that can be misleading in the case of magnetic control. This use of "efficiency" relates to how much forward velocity results from a given propeller movement, but does not account for the power that is required to generate said movement. In the case of constant-power swimming, the presence of walls typically tends to decrease swimming speed in microorganisms (Lauga and Powers 2009). In our case of constant magnetic torque input, we can expect power input to decrease with increased fluid drag, since power input is the product of torque and angular velocity, and angular velocity will reduce with increased drag for a given torque. In addition, the magnetic head will experience an increase in fluid drag similar to the gradient-pulled bead. Consequently, we should expect a decrease

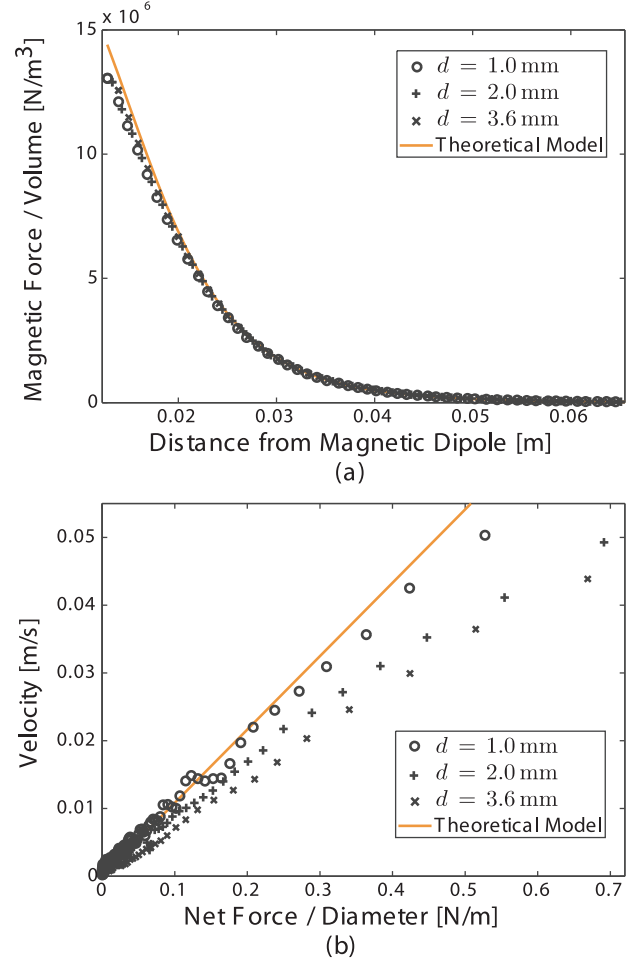


Fig. 10. Experimental results for three steel beads using the custom measurement system of Kummer et al. (2007). Data originally appeared in Erganeman et al. (2008). (a) Magnetic forces are accurately predicted using a theoretical model. (b) Hydrodynamic predictions of the beads being pulled through silicon oil ($\rho = 970 \text{ kg m}^{-3}$, $\eta = 0.98 \text{ Pa}\cdot\text{s}$) are less accurate, as Stokes-flow equations do not accurately account for wall effects of the 26-mm-diameter container.

in swimming speed near solid boundaries for both the helical-propeller and elastic-tail microrobots.

3. Our swimming models and critical comparison all consider one-degree-of-freedom motion. In practice, it will be necessary to steer the microrobots while creating propulsion, and the coupled relationship between magnetic steering and propulsion is not always trivial. In addition, the helical swimmer and the elastic-tail swimmer must use non-holonomic steering techniques, whereas gradient pulling has the potential for control authority in every direction. Walls also affect steering. As viscous drag increases nearer to a wall, rotating bodies tend to

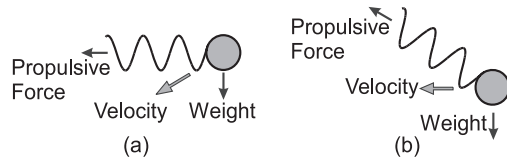


Fig. 11. (a) Simple helical propulsion results in drift due to gravity. (b) Swimming similar to helicopter flight can counteract gravity.

roll along walls, even when there is no direct contact. It is known that some bacteria tend to swim in circles near solid boundaries, which is due to the counter-rotation of the bacterium and its flagellum, each tending to roll along the wall in opposite directions, resulting in a net torque (Lauga et al. 2006). We have observed an analogous behavior in the magnetic helical microswimmers of Figure 9: they tend to drift sideways along a solid boundary as they move forward, rather than swim in circles, because the magnetic head and the helical propeller do not counter-rotate.

4. There is another factor that must be considered in micro-robot swimming: gravity. It is often claimed that inertia is negligible at low Re , but “inertia” is used differently here than “mass”. A microrobot will reach its terminal velocity in a fluid nearly instantaneously, and the terminal velocity decreases with size. However, even at low Re , a microrobot will still fall downward under its own weight. The propulsion models developed in Sections 5 and 6 assume that flow is along the axis of the propeller. However, this only provides for propulsion along the axis, which will be insufficient to counteract gravity when swimming horizontally, as shown in Figure 11(a). It may be necessary to swim with an angle of attack, as shown in Figure 11(b), and we have, in fact, experimentally found this to be the case (Zhang et al. 2009). Microorganisms that swim using flagella have a density similar to water, and are thus nearly neutrally buoyant, making this effect of gravity on propulsion unique to microrobots that are constructed of denser-than-water materials.
5. It is possible to combine the benefits of field gradients with those of helical propulsion or elastic-tail propulsion. That is, we can pull as we rotate. This hybrid method has the potential for improved performance, and may be particularly useful in counteracting the effect of gravity. However, it will require a more complicated actuation scheme than that considered in Figure 7(a).
6. Helical-propulsion models typically assume a perfectly rigid helix. In Figure 12 we show experimental data for

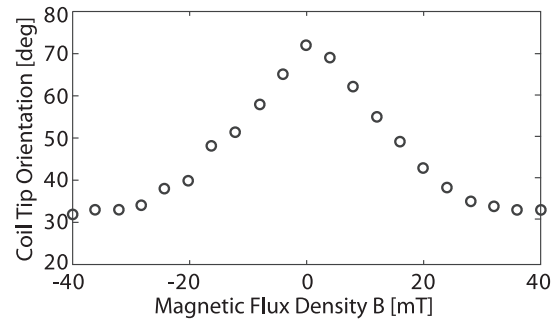


Fig. 12. A nanocoil attached to the chip, similar to that shown in Figure 9(c), is subjected to a magnetic torque and characterized as a spring in Bell et al. (2007).

a nanocoil still attached to the chip, like that seen in Figure 9(c), subjected to a magnetic field and behaving like a spring; the nanocoil is clearly not rigid. The characterization of the stiffness of the helical propellers (Bell et al. 2006) can be used for improved helical-propulsion models.

Finally, it would be interesting to compare another type of magnetic propulsion scheme with the three methods presented in this paper. Dreyfus et al. (2005) assembled a chain of paramagnetic beads, interconnected by DNA, which, when attached to a body, can be used for propulsion. The microrobot is propelled by an oscillating magnetic field, and the hardware requirements for magnetic field generation are the same as that for elastic-tail propulsion. The oscillating field induces something like a wave in the chain that travels from the distal end toward the body, resulting in a propeller that pulls the body behind it, as opposed to the elastic tail, which pushes the magnetic body. One desirable property of this type of propulsion is that the attached body can be any payload, and does not itself need to be magnetic in any way (in Dreyfus et al. (2005) they pull a red blood cell). An undesirable property of this type of propulsion is that the chain of paramagnetic beads theoretically requires an attached body for any propulsion to occur. Subsequent work has shown that defects in the chain can create the asymmetry needed to break the “scallop theorem” and result in some net movement without an attached body (Roper et al. 2006). However, it is not clear how such a defect would affect the swimming efficiency with an attached body. It is also not clear how well the fabrication of these microswimmers, which was successfully performed at very small scales under a microscope, scales up to the type of microrobot dimensions that might be of more practical use for *in vivo* medical applications. A critical comparison of the Dreyfus microswimmer with other common microswimming methods is an interesting topic for future consideration, and a recent work (Roper et al. 2008) may form the basis for such a comparison.

9. Conclusions

Magnetic fields provide an unequalled means of wireless power and control for microrobots. However, the strength of magnetic fields and field gradients decreases rapidly with distance from the source, which has a profound impact on the best way to make use of these fields for microrobot propulsion. Although it has been previously observed that a swimming microrobot with a helical propeller is far less efficient than simply pulling the microrobot through the fluid, we find that a helical propeller is far superior to pulling if we consider the limitations of magnetic field sources. We find that optimal performance of helical propellers and elastic tails are very comparable. We find that both generally become preferable to pulling with field gradients as microrobot size decreases or as the distance from the magnetic field sources increases. Considering additional practical considerations, we made the case that helical propulsion will likely be the best choice for *in vivo* applications. However, the design of hardware that realizes the theoretical possibilities of any of the propulsion methods remains a challenging problem.

Acknowledgments

This work was presented in part at the 2007 International Symposium of Robotics Research. This work is supported in part by the NCCR Co-Me of the Swiss National Science Foundation. The authors would like to thank Haixin Zhang for technical help in the experiments shown in Figure 9(d), and Michael Kummer for technical assistance in collecting the data in Figure 10.

References

- Abbott, J. J., Ergeneman, O., Kummer, M. P., Hirt, A. M. and Nelson, B. J. (2007). Modeling magnetic torque and force for controlled manipulation of soft-magnetic bodies. *IEEE Transactions on Robotics*, **23**(6): 1247–1252.
- Behkem, B. and Sitti, M. (2006). Design methodology for biomimetic propulsion of miniature swimming robots. *ASME Journal of Dynamic Systems, Measurement, and Control*, **128**: 36–43.
- Bell, D. J., Dong, L. X., Nelson, B. J., Golling, M., Zhang, L. and Grützmacher, D. (2006). Fabrication and characterization of three-dimensional InGaAs/GaAs nanosprings. *Nano Letters*, **6**: 725–729.
- Bell, D. J., Leutenegger, S., Hammar, K. M., Dong, L. X. and Nelson, B. J. (2007). Flagella-like propulsion for microrobots using a magnetic nanocoil and rotating electromagnetic field. *Proceedings of the IEEE International Conference on Robotics and Automation*, pp. 1128–1133.
- Brennen, C. and Winet, H. (1977). Fluid mechanics of propulsion by cilia and flagella. *Annual Review of Fluid Mechanics*, **9**: 339–398.
- Cosentino Lagomarsino, M., Capuani, F. and Lowe, C. P. (2003). A simulation study of the dynamics of a driven filament in an Aristotelian fluid. *Journal of Theoretical Biology*, **224**: 215–224.
- Dreyfus, R., Baudry, J., Roper, M. L., Fermigier, M., Stone, H. A. and Bibette, J. (2005). Microscopic artificial swimmers. *Nature*, **437**(6): 862–865.
- Ergeneman, O., Dogangil, G., Kummer, M. P., Abbott, J. J., Nazeeruddin, M. K. and Nelson, B. J. (2008). A magnetically controlled wireless optical oxygen sensor for intraocular measurements. *IEEE Sensors Journal*, **8**(1): 29–37.
- Grady, M. S., Howard, M. A., III, Molloy, J. A., Ritter, R. C., Quate, E. G. and Gillies, G. T. (1990). Nonlinear magnetic stereotaxis: three-dimensional, *in vivo* remote magnetic manipulation of a small object in canine brain. *Medical Physics*, **17**(3): 405–415.
- Guo, S., Pan, Q. and Khamesee, M. B. (2008). Development of a novel type of microrobot for biomedical application. *Microsystem Technologies*, **14**: 307–314.
- Honda, T., Arai, K. I. and Ishiyama, K. (1996). Micro swimming mechanisms propelled by external magnetic fields. *IEEE Transactions on Magnetics*, **32**(5): 5085–5087.
- Ishiyama, K., Arai, K. I., Sendoh, M. and Yamazaki, A. (2003). Spiral-type micro-machine for medical applications. *Journal of Micromechatronics*, **2**(1): 77–86.
- Jiles, D. (1991). *Introduction to Magnetism and Magnetic Materials*. London, Chapman and Hall.
- Kósa, G., Jakab, P., Jólesz, F. and Hata, N. (2008). Swimming capsule endoscope using static and RF magnetic field of MRI for propulsion. *Proceedings of the IEEE International Conference on Robotics and Automation*, pp. 2922–2927.
- Kósa, G., Shoham, M. and Zaaroor, M. (2007). Propulsion method for swimming microrobots. *IEEE Transactions on Robotics*, **23**(1): 137–150.
- Kummer, M. P., Abbott, J. J., Vollmers, K. and Nelson, B. J. (2007). Measuring the magnetic and hydrodynamic properties of assembled-MEMS microrobots. *Proceedings of the IEEE International Conference on Robotics and Automation*, pp. 1122–1127.
- Lauga, E., DiLuzio, W. R., Whitesides, G. M. and Stone, H. A. (2006). Swimming in circles: motion of bacteria near solid boundaries. *Biophysical Journal*, **90**: 400–412.
- Lauga, E. and Powers, T. R. (2009). The hydrodynamics of swimming microorganisms. *Reports on Progress in Physics* (accepted).
- Li, H., Tan, J. and Zhang, M. (2006). Dynamics modeling and analysis of a swimming microrobot for controlled drug delivery. *Proceedings of the IEEE International Conference on Robotics and Automation*, pp. 1768–1773.
- Lighthill, J. (1976). Flagellar hydrodynamics. *SIAM Review*, **18**(2): 161–230.

- Mathieu, J.-B., Beaudoin, G. and Martel, S. (2006). Method of propulsion of a ferromagnetic core in the cardiovascular system through magnetic gradients generated by an MRI system. *IEEE Transactions on Biomedical Engineering*, **53**(2): 292–299.
- Meeker, D. C., Maslen, E. H., Ritter, R. C. and Creighton, F. M. (1996). Optimal realization of arbitrary forces in a magnetic stereotaxis system. *IEEE Transactions on Magnetics*, **32**(2): 320–328.
- Nagy, Z., Erganeman, O., Abbott, J. J., Hutter, M., Hirt, A. M. and Nelson, B. J. (2008). Modeling assembled-MEMS microrobots for wireless magnetic control. *Proceedings of the IEEE International Conference on Robotics and Automation*, pp. 874–879.
- Purcell, E. M. (1977). Life at low Reynolds number. *American Journal of Physics*, **45**(1): 3–11.
- Purcell, E. M. (1997). The efficiency of propulsion by a rotating flagellum. *Proceedings of the National Academy of Sciences of the United States of America*, **94**: 11307–11311.
- Roper, M., Dreyfus, R., Baudry, J., Fermigier, M., Bibette, J. and Stone, H. A. (2006). On the dynamics of magnetically driven elastic filaments. *Journal of Fluid Mechanics*, **554**: 167–190.
- Roper, M., Dreyfus, R., Baudry, J., Fermigier, M., Bibette, J. and Stone, H. A. (2008). Do magnetic micro-swimmers move like eukaryotic cells? *Proceedings of the Royal Society A*, **464**: 877–904.
- Sendoh, M., Ishiyama, K. and Arai, K.-I. (2003). Fabrication of magnetic actuator for use in a capsule endoscope. *IEEE Transactions on Magnetics*, **39**(5): 3232–3234.
- Sudo, S., Segawa, S. and Honda, T. (2006). Magnetic swimming mechanism in a viscous liquid. *Journal of Intelligent Material Systems and Structures*, **17**: 729–736.
- Vogel, S. (2003). *Comparative Biomechanics: Life's Physical World*. Princeton, NJ, Princeton University Press.
- White, F. M. (1991). *Viscous Fluid Flow* (2nd edition). New York, McGraw-Hill.
- Wiggins, C. H. and Goldstein, R. E. (1998). Flexive and propulsive dynamics of elastica at low Reynolds number. *Physical Review Letters*, **80**(17): 3879–3882.
- Wiggins, C. H., Riveline, D., Ott, A. and Goldstein, R. E. (1998). Trapping and wiggling: elasto-hydrodynamics of driven microfilaments. *Biophysical Journal*, **74**: 1043–1060.
- Yesin, K. B., Vollmers, K. and Nelson, B. J. (2006). Modeling and control of untethered biomicrobots in a fluidic environment using electromagnetic fields. *The International Journal of Robotics Research*, **25**(5–6): 527–536.
- Yu, T. S., Lauga, E. and Hosoi, A. E. (2006). Experimental investigations of elastic tail propulsion at low Reynolds number. *Physics of Fluids*, **18**: 091701.
- Zhang, L., Abbott, J. J., Dong, L. X., Kratochvil, B. E., Bell, D. and Nelson, B. J. (2009). Artificial bacterial flagella: fabrication and magnetic control. *Applied Physics Letters*, **94**: 064107.